Magnetic impurities as the origin of the variability in spin relaxation rates in Cu-based spin transport devices

J. D. Watts,[1,2,*] L. O'Brien,[3,*] J. S. Jeong,[2] K. A. Mkhoyan,[2] P. A. Crowell,[1] and C. Leighton[2,†]
[1]School of Physics and Astronomy, University of Minnesota, Minnesota 55455, USA
[2]Department of Chemical Engineering and Materials Science, University of Minnesota, Minnesota 55455, USA
[3]Department of Physics, University of Liverpool, Liverpool L69 7ZE, United Kingdom

(Received 9 September 2019; published 23 December 2019)

The Elliott-Yafet spin relaxation mechanism posits linear proportionality between spin and momentum lifetimes in low spin-orbit coupling nonmagnetic metals, and is widely accepted in spintronics. Accurate experimental determination of the Elliott-Yafet proportionality constants (β_i) between the spin and momentum relaxation times for individual scattering sources is challenging, however. This is apparent from the literature on nonlocal spin transport in Cu, for example, where reported phonon ($\beta_{\rm ph}$) and defect ($\beta_{\rm def}$) Elliott-Yafet constants vary by an order of magnitude. In recent work we discovered that even part-per-million-level magnetic impurity concentrations can substantially influence spin relaxation in Cu, via a spin transport analog of the Kondo effect. To clarify whether this could explain the reported variability in β_i, here we report on a comprehensive study of spin transport in Cu-based lateral nonlocal spin valves, varying the ferromagnetic contact material, interface structure, Cu thickness, and post-fabrication annealing conditions, resulting in widely varied microstructures and magnetic impurity concentrations. Quantifying the effects of magnetic impurities on charge and spin transport we demonstrate the dramatic, even dominant, effect these can have on spin relaxation rates, and thus extracted β_i. Minimization of magnetic impurity effects is achieved via Al interlayer insertion or moderate annealing, restoring the expected temperature dependence for phonon-mediated spin relaxation, and enabling more reliable determination of β_i for phonons (740 ± 200), and nonmagnetic defects (240 ± 50). The latter contribution is shown to be dominated by grain boundaries in these polycrystalline Cu films. Cross-sectional transmission electron microscopy measurement of grain sizes in actual nonlocal spin valve devices then establishes a useful empirical relationship between average grain size and spin diffusion length. These measurements highlight the importance of magnetic impurities in metallic spin transport, explain the wide variability in reported $\beta_{\rm ph}$ and $\beta_{\rm def}$ in Cu, and elucidate the relationship between metallic spin transport and microstructure.

DOI: 10.1103/PhysRevMaterials.3.124409

I. INTRODUCTION

Efficient and controlled transport of spins in metals would enable numerous advances in spintronic devices, including sensors, logic, and data storage devices. One specific example is the need for metal-based alternatives to magnetic tunnel junctions in hard disk drive read head sensors, which arises due to resistance scaling challenges at low dimensions [1–3]. The substantial effort to improve our understanding of the injection of spins from ferromagnetic (FM) to nonmagnetically-ordered ("nonmagnetic," NM) metals, and their subsequent transport and relaxation, thus continues, particularly at nano- and meso-scopic scales [4–22]. Among the many questions that remain open, the impact of specific scattering sources on spin relaxation in NM metals is prominent [11,21,23–25]. Even in heavily studied light metals with weak spin-orbit interaction (e.g., Al, Cu), the individual effects of interfaces, surfaces, grain boundaries, dislocations, and point defects (impurities, etc.) are far from understood [9,11,17–19,21,26–28].

The prevailing theoretical picture for spin relaxation in light NM metals, widely accepted in spintronics, is the Elliott-Yafet (E-Y) mechanism, wherein conventional elastic scattering mediates spin mixing, controlled by the spin-orbit interaction strength [29–31]. This was originally cast in terms of simple linear proportionality between the spin lifetime τ_s and the momentum relaxation time τ_e, i.e., $\tau_s = \beta\tau_e$, where β is sometimes referred to as an E-Y constant [32]. Following a probabilistic interpretation, spin relaxation thus occurs every β momentum relaxation events on average (i.e., with probability β^{-1} at each event), β being proportional to the spin-orbit interaction strength. This original formulation did not, however, explicitly account for multiple possible sources of scattering, such as phonons, surfaces, grain boundaries, impurities, etc. To address this, a generalized E-Y relation was advanced [6,7,9–11,13–15,18–21], essentially applying Mattheissen's rule to spin transport. The total spin relaxation rate then becomes

$$\frac{1}{\tau_s} = \sum_i \frac{1}{\tau_{s,i}} = \sum_i \frac{1}{\beta_i}\,\frac{1}{\tau_{e,i}}, \tag{1}$$

where the $1/\tau_{s,i}$ are the individual spin relaxation rates due to scattering source i, the $1/\tau_{e,i}$ are the corresponding

*These authors contributed equally to this work.
†Corresponding author: leighton@umn.edu

individual momentum relaxation rates, and the β_i are the E-Y constants for each source of scattering. Framed this way, the challenge of quantitative understanding of metallic spin relaxation reduces to determining the important β_i in a given NM, for subsequent comparison with theory. *Some* successes have been achieved. Elemental NM metals such as Au, Cu, Ag, Na, and K, for example, were shown from conduction electron spin resonance (CESR) measurements to have the temperature (T)-dependent scaling of $1/\tau_s$ with resistivity (ρ) expected from Eq. (1) [32]. More recently, the phonon value of β ($\beta_{\rm ph}$) in polyvalent Al was quantitatively understood in terms of "spin hot spots," i.e., points on the Fermi surface where spin-orbit coupling becomes strong compared to interband energies [33,34]. In general, however, quantitative experimental determination of even the most elementary β_i in Eq. (1) has proven challenging. Historically, there has been a paucity of methods to accurately determine τ_s for comparison to τ_e, particularly with some means to separate scattering sources such as phonons and T-independent defects. Historical literature data for β are thus mostly restricted to $\beta_{\rm ph}$ values from CESR on ultrapure NMs [30,32,35]. In Cu, for example, this has led to an accepted value for $\beta_{\rm ph}$ of ∼1000, meaning that spin relaxation occurs every ∼1000 phonon scattering events on average [30,32].

In principle, the lateral nonlocal spin valve (NLSV) provides a means to substantially advance the quantitative understanding of E-Y spin relaxation in metals, as it enables all-electrical generation and detection of diffusive pure spin currents [4,5]. This allows for determination of $\tau_s(T)$ in a device in which $\rho(T)$, and thus $\tau_e(T)$, can also be straightforwardly measured. Appropriate analysis then enables separation of T-dependent (phonon) scattering from T-independent (defect) scattering, thus determining $\beta_{\rm ph}$ and $\beta_{\rm def}$. Additional experiments carefully varying specific defect densities could then be used to deconvolute the effects of various defects (e.g., grain boundaries, surfaces, impurities, etc.) on $\beta_{\rm def}$.

Briefly, the NLSV geometry places two FM nanowire contacts (a spin injector and a spin detector) a distance d apart on an NM nanowire channel, as schematically shown in Fig. 1(a). Injection of a current I from the injector FM into the NM wire results in accumulation of a nonequilibrium spin population in the NM. This spin population diffuses towards the detector FM where it is detected via the nonlocal potential difference $\Delta V_{\rm NL}$ that develops between the detector FM and the far end of the NM wire, which remains in equilibrium. This $\Delta V_{\rm NL}$ is measured by toggling the magnetizations of the injector and detector between parallel (V_P) and antiparallel ($V_{\rm AP}$) states. The nonlocal spin resistance, or "spin signal" is then given by $\Delta R_{\rm NL} = \Delta V_{\rm NL}/I$, providing a direct measure of the spin accumulation at the detector. T-dependent measurements of $\Delta R_{\rm NL}$ vs d then yield the NM spin diffusion length $\lambda_N(T)$ and thus $\tau_s(T)$. This can be compared with $\tau_e(T)$ determined from $\rho(T)$, enabling the determination of $\beta_{\rm ph}$ (from the T dependence) and $\beta_{\rm def}$ (from the low T, residual values).

Although the above analysis appears relatively straightforward, examination of the literature on metallic NLSVs reveals remarkable variability in published $\beta_{\rm ph}$ and $\beta_{\rm def}$ values. Cu, Al, and Ag are the only NM metals that have been widely studied in NLSVs, Cu being the focus of most attention [10,11,13–15,18–20]. Even in this most heavily studied case,

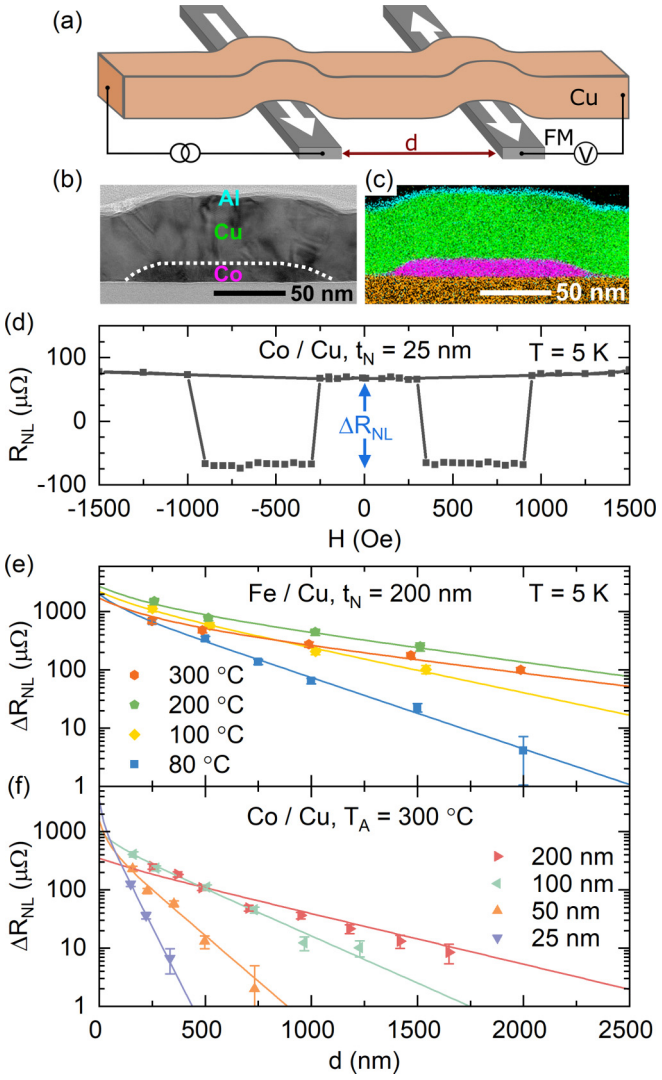

FIG. 1. (a) Schematic of the NLSV geometry for a FM/Cu device, showing the Cu channel, FM injector/detector (with separation d), and nonlocal measurement configuration. (b) Cross-sectional TEM image of a Co/Cu NLSV, showing the Co injector and Cu channel ($t_N = 50$ nm). (c) Corresponding STEM/EDX chemical composition map (magenta, Co; cyan, Al; green, Cu). (d) Nonlocal resistance ($R_{\rm NL}$) vs H for a $t_N = 25$ nm Co/Cu NLSV at $T = 5$ K; the spin accumulation signal ($\Delta R_{\rm NL} = R_P - R_{\rm AP}$) is indicated. (e) and (f) $\Delta R_{\rm NL}$ vs d at temperature $T = 5$ K. Note the semilog scale. Data are shown for: (e) Fe/Cu NLSVs with channel thickness $t_N = 200$ nm annealed at temperatures T_A between 80 and 300 °C and (f) Co/Cu NLSVs with $T_A = 300$ °C at t_N between 25 and 200 nm. Solid lines are fits to the model described in the text. Error bars are shown but in some cases are smaller than the data points.

reported $\beta_{\rm ph}$ values for Cu vary between 490 and 3570 [10,13–15,20], i.e., almost an order-of-magnitude. Although this range encompasses the accepted CESR value of ∼1000 [30,32], it is unclear what the origin of the large variability in NLSV-deduced $\beta_{\rm ph}$ values is, and thus what level of agreement truly exists between CESR and NLSV measurements. The situation is similarly unsatisfactory for $\beta_{\rm def}$. Reported values for Cu span from 215 to 2560 [10,11,13–15,18–20], i.e., a factor of ∼12, with little understanding of how this

should be apportioned among various possible defects. Some work has attempted to correlate $\beta_{\rm def}$ with grain size, deducing a grain boundary β ($\beta_{\rm GB}$) of ∼1000 [11], but other specific defect β_i remain unknown. Moreover, given that the reported ranges for $\beta_{\rm ph}$ and $\beta_{\rm def}$ overlap, it is not clear if these values truly differ in Cu. Given these questions, it is imperative that some understanding be gained of the root cause of the wide variability in E-Y β values from metallic NLSV studies.

A range of factors have been suggested to play a role in the variability of NLSV-deduced $\beta_{\rm ph}$ and $\beta_{\rm def}$ values in metals such as Cu, including strong and/or T-dependent surface spin relaxation [7,19,21,22], variation in deposition conditions (generating variable distributions of defect types) [8,12], and uncontrolled incorporation of large spin-orbit coupling impurities [36]. A quite different factor recently discovered to play a striking role in metallic spin transport is incorporation of *magnetic* impurities (MIs). Specifically, recent work from ourselves [28,37–39] and others [6,11,13,40] demonstrated that even very low concentrations of MIs [order parts-per-million (ppm)] can dramatically influence metallic spin transport through a manifestation of the Kondo effect. Early work on this effect noted that the widely observed unexpected nonmonotonicity in $\Delta R_{\rm NL}(T)$ in Cu-based NLSVs occurs due to a low T suppression of $\Delta R_{\rm NL}$ that is logarithmic in T, with a characteristic temperature in good agreement with the known Kondo temperature (T_K) of the FM/Cu pairing [28]. The nonmonotonicity in $\Delta R_{\rm NL}(T)$ was also found to vanish in NLSVs based on Al, a metal that is known to not support local moments on dilute 3d transition metal impurities, and thus not exhibit the Kondo effect [41–43]. Subsequent analyses demonstrated that the low T decrease in $\Delta R_{\rm NL}(T)$ occurs due to logarithmic suppression of the current spin polarization α [28,39]. This was explained in terms of depolarization of the injected spin current by Kondo scattering at MIs near the interface, generated by FM/NM interdiffusion. Annealing was shown to enhance this interdiffusion, leading to simultaneous observation of conventional transport and spin transport Kondo effects, and quantification of channel MI concentrations (in the 10–100 ppm range) [37]. Subsequent work also introduced MIs *throughout* the channel, rather than only at the FM/NM interface, resulting in similar Kondo effects not only in $\alpha(T)$, but directly in $\tau_s(T)$ and $\lambda_N(T)$ [13]. Accompanying theory was then developed, showing, remarkably, that although the process is not spin-orbit mediated, Kondo spin relaxation at MIs can be cast in E-Y form, i.e., $\tau_{s,K} = \beta_K \tau_{e,K}$ (where the "K" subscript denotes Kondo), with $\beta_K = 3/2$ [39]. This remarkably low effective E-Y β value (compare $\beta_K = 3/2$ with $\beta_{\rm ph} \approx 1000$ in Cu for example) was then validated experimentally [38,39], confirming that spin relaxation at MIs is highly efficient compared to spin-orbit-mediated relaxation at NM defects. Spin transport is thus even more sensitive than charge transport to ppm-level MI concentrations. Given this demonstrated importance of MIs in Cu, it is natural to ask whether Kondo spin relaxation could play a role in the variability in $\beta_{\rm ph}$ and $\beta_{\rm def}$ in Cu-based NLSVs. This is the motivation for this work. Importantly, based on these recent experimental and theoretical developments, we are now armed with the capability to fully *quantify* the influence of MIs on both charge and spin transport.

With these goals in mind, we report here on a comprehensive study of spin transport in Cu-based NLSVs, varying the FM contact material, interface structure (either FM/Cu or FM/Al interlayer/Cu), Cu channel thickness, and post-fabrication annealing conditions, achieving widely varied microstructures, interdiffusion levels, and channel MI concentrations. Quantifying MI effects on charge and spin transport, we demonstrate the significant, even dominant, effect these can have on spin relaxation. In the worst cases the expected T dependence of τ_s is in fact completely masked by Kondo scattering, rendering extraction of reliable β_i impossible. Minimization of MI effects is achieved via Al interlayer insertion or moderate annealing, however, restoring the expected T dependence of τ_s and enabling more reliable determination of $\beta_{\rm ph} = 740 \pm 200$ and $\beta_{\rm def} = 240 \pm 50$. Grain boundaries are then shown to be the dominant contributor to $\beta_{\rm def}$, cross-sectional transmission electron microscopy (TEM) measurement of grain sizes in actual NLSVs establishing a useful empirical relationship between average grain size and λ_N in Cu. These measurements and analyses highlight the importance of MIs in metallic spin transport, explain the wide variability in reported $\beta_{\rm ph}$ and $\beta_{\rm def}$ in Cu-based NLSVs, and elucidate the relationship between metallic spin transport and microstructure.

II. EXPERIMENTAL METHODS

NLSVs were fabricated with Cu channels, using Fe, Co, and $Ni_{80}Fe_{20}$ (permalloy, Py) as the FM contacts. Shadow masks defined by electron beam lithography on Si/Si-N substrates were used for multiangle deposition of NLSVs, as in our prior work [28,37–39,44]. Ultrahigh vacuum (∼10^{-10} Torr base pressure) electron beam evaporation was employed, with Cu source purity of 99.999% and FM purity of 99.95%. Deposition rates for Cu and the FMs were kept at 1.0 and 0.5 Å s^{-1}, respectively; the FM thickness (t_F) was held at 16 nm, while the Cu thickness (t_N) was varied between 25 and 400 nm. The widths of the FM injector, FM detector, and NM channel were fixed at 100, 150, and 200 nm, respectively, and the injector-detector separation (d) was varied between 150 and 2000 nm. As discussed below, some NLSVs also had a 6 nm Al interlayer (IL) between the FM and NM, and some devices (Fe/Cu) were annealed, post-fabrication, at temperatures T_A up to 500 °C in vacuum (10^{-6} Torr) for 2 h. Unannealed devices reach 80 °C during processing, and are thus labeled as $T_A = 80$ °C. Conventional cross-sectional TEM imaging was conducted using an aberration-corrected (probe-corrected) FEI Titan G2 60–300 scanning TEM (STEM), operated at 300 kV. Cross-sectional TEM specimens were prepared using a focused ion beam (FIB, FEI Helios NanoLab G4) using 30 kV Ga ions, followed by 1–5 kV ion milling to remove damaged layers on the specimen surfaces. An example TEM image from a Co/Cu NLSV, with $t_N = 50$ nm, is shown in Fig. 1(b), along with a corresponding energy-dispersive x-ray (EDX) spectroscopy composition map in Fig. 1(c) (color map: magenta, Co; green, Cu; cyan, Al). Examining Figs. 1(b) and 1(c), the 16 nm thick Co injector and conformal Cu channel are readily seen. NLSV electrical measurement methods have also been described in prior work [28]. Briefly, 13 Hz AC excitation was employed, using typical currents of 316 μA.

Measurements were made from 5 to 275 K, $\Delta R_{\rm NL}$ being determined from in-plane magnetic field sweeps at each T.

III. RESULTS

A. Extraction of spin diffusion lengths and lifetimes

Two sets of NLSVs form the basis for the majority of this study: an Fe/Cu set with fixed $t_N = 200$ nm and varied T_A (80 to 500 °C) and a Co/Cu set with fixed $T_A = 300$ °C and varied t_N (25 to 200 nm). (An additional set of devices discussed in later sections is based on Py/Cu with $T_A =$ 80 °C and $t_N =$ 200–400 nm.) Figure 1(d) displays a typical measurement of $R_{\rm NL}(H)$ for our devices, in this case a Co/Cu NLSV with $t_N = 50$ nm, measured at $T = 5$ K. Indicated in the figure is the spin accumulation signal $\Delta R_{\rm NL} = R_P - R_{\rm AP}$. Note, as is typical throughout the literature, that a field-independent "background" (2.27 mΩ in this case) has been removed from the data of Fig. 1(d). Figures 1(e) and 1(f) show illustrative $T = 5$ K (semilog) plots of $\Delta R_{\rm NL}$ vs d for the two primary sample sets. Considering Fig. 1(e), the expected simple exponential decay of $\Delta R_{\rm NL}(d)$ is evident at high d, directly reflecting the magnitude of λ_N, which apparently increases with T_A and t_N [Figs. 1(e) and 1(f), respectively]. Also apparent in Fig. 1(e) are the typical low d deviations from simple exponential behavior. These are characteristic of transparent (i.e., low resistance) FM/NM interfaces, occurring due to back-diffusion of injected spins into the FMs [45]. As illustrated by the solid fit lines, the full d dependence is well described by the 1D magnetoelectronic circuit theory solution for $\Delta R_{\rm NL}$ in the NLSV geometry in the transparent interface limit [45,46]:

$$\Delta R_{\rm NL}(d,T) = 4\frac{{\alpha_{\rm eff}}^2 {R_{\rm FM}}^2}{(1-{\alpha_{\rm eff}}^2)^2 R_N}\frac{\exp(-d/\lambda_N)}{\left[1+\frac{2R_{\rm FM}}{(1-{\alpha_{\rm eff}}^2)R_N}\right]^2-\exp(-2d/\lambda_N)}. \quad (2)$$

Here $R_N = \rho_N\lambda_N/w_N t_N$ and $R_F = \rho_F\lambda_F/w_N w_F$ are the spin resistances in the NM and FM, ρ_N and ρ_F are the respective resistivities, λ_N and λ_F are the respective spin diffusion lengths, and w_N and w_F are the respective widths. As in our prior work [28,37–39,44], we employ an effective value of the current spin polarization $\alpha_{\rm eff}$ to account for depolarization of the injected spin current by Kondo scattering at interdiffused FM/NM interfaces. In order to best constrain the fitting, resistivities were measured on the same NLSVs (or on nanowires with identical dimensions in the case of the FMs), all dimensions were measured for each device, and λ_F was constrained to a T-independent value of 4 nm, derived from empirical scaling with ρ_F [47]. This leaves only λ_N and $\alpha_{\rm eff}$ as fitting parameters, the former being uniquely determined by the high d exponential behavior. Close inspection of Figs. 1(e) and 1(f) suggests complex T_A and t_N evolution of the slope and intercept, and thus λ_N and $\alpha_{\rm eff}$, as discussed quantitatively below.

Fitting results for $\lambda_N(T)$ and $\alpha_{\rm eff}(T)$ are summarized in Fig. 2, for both the variable T_A Fe/Cu NLSVs (left panel) and the variable t_N Co/Cu NLSVs (right panel). Also shown for comparison in Fig. 2 are $\tau_e(T)$ and $\tau_s(T)$, for the same devices. $\tau_e(T)$ is extracted from $\rho_N(T)$ measured on the exact same NLSVs, using $\tau_e(T) = 3/\rho_N(T)N(E_F)e^2{v_F}^2$, i.e., standard Boltzmann transport [48], where $N(E_F)$ denotes the density-of-states at the Fermi level and v_F is the Fermi velocity. $\tau_s(T)$, on the other hand, is extracted from $\lambda_N(T)$ via the typical relations $\tau_s = {\lambda_N}^2/D$ and $D = v_F/\sqrt{3\tau_e}$. Figures 2(a) and 2(e) first show $\tau_e(T)$, and its response to T_A and t_N, from which some simple deductions can be made. From Fig. 2(e), τ_e can be seen to trend towards a weakly thickness-dependent value at high T, consistent with phonon scattering. In the low T limit, however, τ_e increases monotonically with t_N, exceeding 100 fs at $t_N = 200$ nm. This reflects the typical finite size scaling of $\rho_N(T)$ in metals, which will be shown below to be dominated by increasing defect (grain boundary) scattering at low t_N. τ_e is also monotonic with T at each t_N [i.e., $\rho_N(T)$ is monotonic], indicating that conventional charge transport Kondo effects are weak. (A minor low T downturn in $\tau_e(T)$ is actually evidenced at 200 nm, consistent with our prior work on Co/Cu [38] and statements in Sec. I.) Moving to the T_A dependence, Fig. 2(a) shows similar overall $\tau_e(T)$ for Fe/Cu, the increase with T_A at low T suggesting an unsurprising decrease in defect density. This holds only up to $T_A = 450$ °C, however, beyond which τ_e drops significantly. Consistent with prior work on Fe/Cu, at $T_A = 500$ °C [37] we then find a small maximum in $\tau_e(T)$ at low T [i.e., a minimum in $\rho_N(T)$], which is evidence of the conventional Kondo effect. As will become clearer below, this is essentially the annealing temperature at which MIs diffuse so extensively throughout the channel that a significant conventional Kondo effect occurs in $\rho_N(T)$ [37].

At first sight, and qualitatively, the trends in the extracted $\lambda_N(T)$ [Figs. 2(b) and 2(f)] appear broadly consistent with expectations based on $\tau_e(T)$, i.e., with E-Y scaling. For most T_A and t_N values, λ_N monotonically increases on cooling, apparently mirroring $\tau_e(T)$. The low T value of λ_N grows with increasing t_N [Fig. 2(f)], and with T_A from 80 to 300 °C [Fig. 2(b)], corresponding to the decreases in defect density deduced from τ_e. Spin diffusion lengths up to almost 1.5 μm are thus obtained. The situation is distinctly more complicated at $T_A \geqslant 400$ °C, however, where clear nonmonotonicity emerges in $\lambda_N(T)$ [see for example the peak in $\lambda_N(T)$ at $T_A = 400$ °C in Fig. 2(b)]. This peak is notably similar to that seen in NLSVs based on low purity Cu [13], suggesting, in agreement with our own prior work on Fe/Cu [37], that at these T_A substantial MI concentrations are present not only at the FM/NM interface (thus affecting $\alpha_{\rm eff}$), but also deep into the channel (thus affecting λ_N). At yet higher T_A the spin diffusion length undergoes a sharp drop, which will be further elucidated below. In general, broad comparison of Figs. 2(a) and 2(e) with Figs. 2(b) and 2(f) suggests qualitative agreement with the E-Y mechanism in that λ_N appears to approximately scale with τ_e, at least until heavy MI contamination of the bulk of the Cu channel sets in.

Interestingly, the simple additional step of directly comparing $\tau_e(T)$ with $\tau_s(T)$ [Figs. 2(c) and 2(g)], rather than $\lambda_N(T)$, exposes obvious problems. These become apparent in Fig. 2(g), for example, where τ_s in Co/Cu NLSVs is found to have remarkably weak T dependence, in most ranges of T and t_N actually *increasing* with increasing T, in obvious contrast with E-Y scaling expectations based on Fig. 2(e). Similar behavior occurs at low T_A in the Fe/Cu NLSVs shown

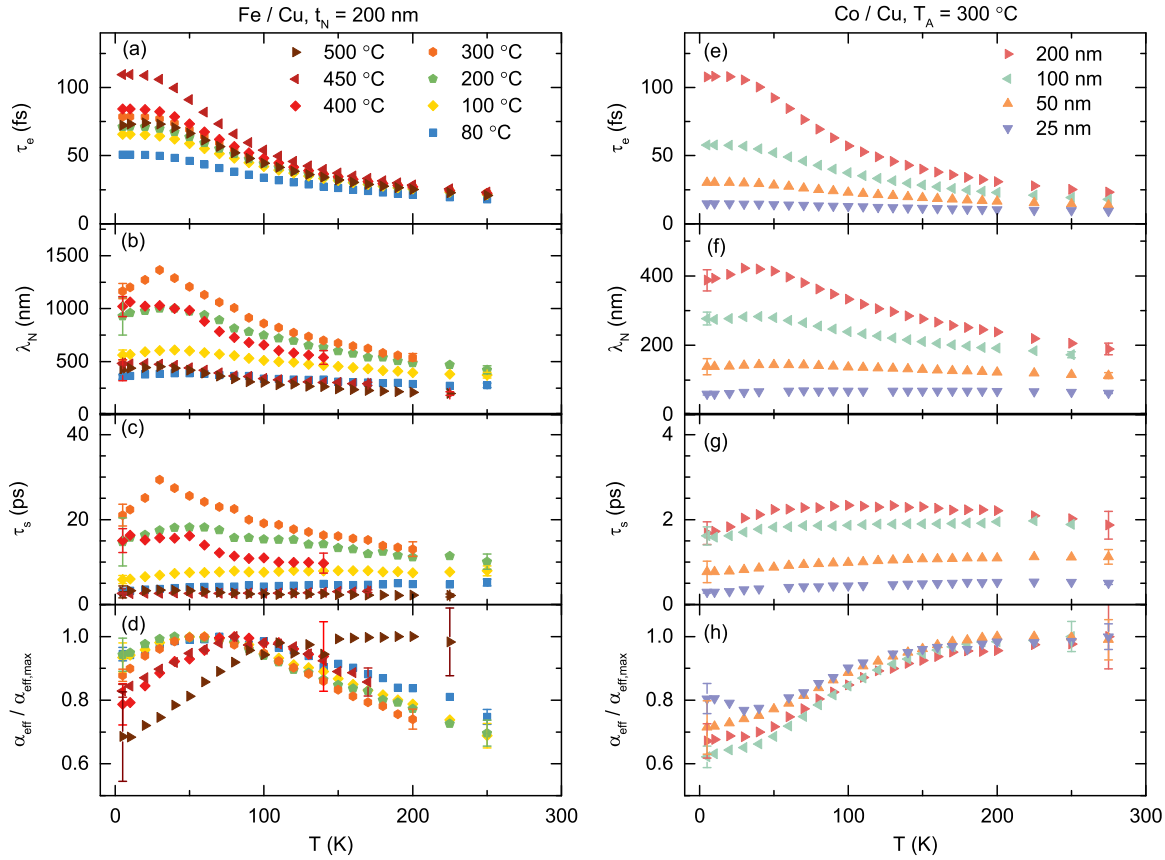

FIG. 2. Temperature (T) dependence of (a) and (e) the elastic scattering time (τ_e), (b) and (f) the spin diffusion length (λ_N), (c) and (g) the spin lifetime (τ_s), and (d) and (h) the effective spin polarization normalized to its maximum value ($\alpha_{\rm eff}/\alpha_{\rm eff,max}$). Data are shown for Fe/Cu NLSVs (left) with fixed channel thickness $t_N = 200$ nm at various annealing temperatures $T_A = 80 - 500\,^{\circ}$C, and for Co/Cu NLSVs (right) at fixed $T_A = 300\,^{\circ}$C and $t_N = 25 - 200$ nm. Error bars are standard errors on extracted fit parameters and are shown only at the highest and lowest T for clarity.

in Fig. 2(c), moderate annealing at around 200–300 °C being required to restore any T window within which τ_s decreases on warming. Increasing T_A to 500 °C then induces a sharp drop in τ_s to just a few ps, comparable to the low values seen in Fig. 2(g) for Co/Cu; this is clearly associated with the corresponding decreases in λ_N [Fig. 2(b)] and τ_e [Fig. 2(a)] at high T_A, occurring due to large MI concentrations accumulating throughout the channel. Before any further analysis, the fact that the spin lifetime in Cu is so different in the Fe/Cu and Co/Cu NLSVs shown in Figs. 2(c) and 2(g) strongly suggests an important role in spin relaxation for interdiffused MIs from the FM.

Figures 2(d) and 2(h) show the final parameter extracted from the fits of the type shown in Fig. 1, i.e., $\alpha_{\rm eff}$. This is plotted as $\alpha_{\rm eff}(T)$ normalized to its maximum value as: (i) this best illustrates the low T downturn due to Kondo suppression of injected polarization at interdiffused interfaces (as discussed in Sec. I); and (ii) the polarization is a property of the FM/NM interface more than the Cu channel (which is the focus here), meaning that the absolute $\alpha_{\rm eff}$ values are of lower interest. The reader may refer to prior work for typical absolute values of $\alpha_{\rm eff}$ [37,38]. The first feature of note in Figs. 2(d) and 2(h) is the aforementioned downturn in $\alpha_{\rm eff}(T)$ at low T, which occurs in all cases. As T_A is increased in Fig. 2(d) this effect strengthens monotonically, to the point where ∼30% of the polarization is lost at low T. This reflects the increasing Fe/Cu interdiffusion with T_A (as studied quantitatively in our prior work [37]), leading to stronger suppression of α by Kondo scattering at interdiffused Fe impurities in the Cu near the interface. Also consistent with prior work, this suppression in polarization shifts dramatically upwards in T for Co/Cu NLSVs [Fig. 2(h)], due to the much larger T_K for Co in Cu (∼ 500 K) compared to Fe in Cu (30 K) [41,49–52]. Due to the constant T_A in the Co/Cu NLSV set, and thus constant extent of interdiffusion, the $\alpha_{\rm eff}/\alpha_{\rm eff,max}(T)$ are rather similar in Fig 2(h).

B. Analysis of spin relaxation rates: Importance of MIs

Based on the above, the behavior of τ_s in these Cu-based NLSVs is clearly anomalous, actually increasing with T over a wide region of parameter space [Figs. 2(c) and 2(g)]. This appears at qualitative odds with E-Y scaling [τ_e monotonically decreases with T in Figs. 2(a) and 2(e)], even prior to the onset of extensive FM/NM interdiffusion at high T_A. To attempt to understand this we now consider the spin relaxation *rate* $\tau_s^{-1}(T)$, applying Eq. (1) to decompose this rate into its dominant components. Figure 3(a) shows $\tau_s^{-1}(T)$ for both

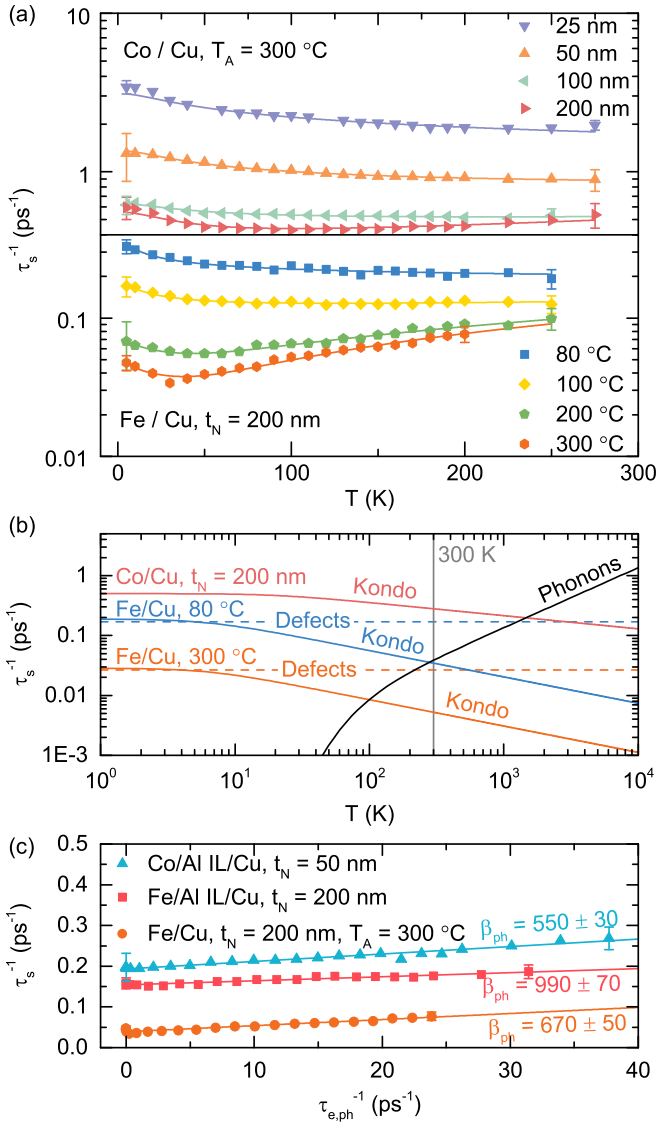

FIG. 3. (a) Temperature (T) dependence of the spin relaxation rate (τ_s^{-1}) for Co/Cu NLSVs (top) with channel thickness $t_N = 25 - 200$ nm and $T_A = 300$ °C, and Fe/Cu NLSVs (bottom) with $t_N = 200$ nm and $T_A = 80 - 300$ °C. Solid lines are fits to the model described in the text, accounting for spin relaxation due to phonons, magnetic impurities, and defects. (b) T dependence of the extracted contributions to τ_s^{-1} in Fe/Cu with $T_A = 80$ and 300 °C, and Co/Cu with $t_N = 200$ nm and $T_A = 300$ °C. The contributions shown are due to Cu phonons (black line, Bloch-Grüneisen model using the average fitted Debye temperature $\theta_D = 300$ K and the phonon Elliott-Yafet constant $\beta_{\rm ph} = 1000$), Kondo magnetic impurities, and T-independent defects (dashed lines). (c) Elliott-Yafet plot, i.e., τ_s^{-1} vs $\tau_{e,\rm ph}^{-1}$, where $\tau_{e,\rm ph}^{-1}$ is the momentum relaxation rate due to phonons. Data are shown for Al interlayer (IL) NLSVs (Co/Al/Cu and Fe/Al/Cu), and a 300 °C annealed Fe/Cu NLSV. The inverse slopes from the straight line fits give the $\beta_{\rm ph}$ values shown. Error bars are standard errors on fit parameters and are shown only at the highest and lowest T for clarity.

Co/Cu and Fe/Cu NLSVs, at various t_N and T_A. For clarity of discussion the extensively interdiffused high T_A samples (400, 450, and 500 °C) are first excluded here, but will be returned to below. Consistent of course with Figs. 2(c) and 2(g), the most striking feature of Fig. 3(a) is the observation of τ_s^{-1} values that decrease on warming, in apparent contradiction to simple expectations based on increasing $\tau_e^{-1}(T)$. Devices such as the $t_N = 25$ nm Co/Cu NLSV in Fig. 3(a) thus appear to yield a spin scattering rate that *decreases with increasing elastic scattering rate,* i.e., an unphysical negative value of $\beta_{\rm ph}$ in Eq. (1). As can be clearly seen in Fig. 3(a), however, the negative slope of $\tau_s^{-1}(T)$ in the 25-nm-thick Co/Cu case is gradually eliminated with increasing t_N and T_A, and on switching from Co to Fe, eventually inverting to positive (i.e., $\beta_{\rm ph} > 0$), at least at sufficiently high T. The anomalous decrease in τ_s^{-1} on warming thus diminishes with decreasing overall spin relaxation rate [from top to bottom in Fig. 3(a)], achieved here through increased t_N and T_A (thus decreased defect density). Given the extensive evidence now gathered for the importance of MIs in metallic spin relaxation [11,13,27,28,37–40,53], one emerging possibility to explain this behavior is that these MIs produce T-dependent spin relaxation that masks the expected phonon contribution, even in the absence of a clear Kondo signature in $\tau_e^{-1}(T)$. Specific evolutions of the MI concentration with t_N, T_A, and the choice of FM, could then potentially explain all aspects of the behavior in Fig. 3(a).

Including phonon, nonmagnetic (T-independent) defect, and MI contributions, Eq. (1) becomes

$$\frac{1}{\tau_s} = \frac{1}{\beta_{\rm ph}}\frac{1}{\tau_{e,\rm ph}} + \frac{1}{\beta_{\rm def}}\frac{1}{\tau_{e,\rm def}} + \frac{1}{\beta_K}\frac{1}{\tau_{e,K}}, \tag{3}$$

where $\tau_{e,\rm ph}$, $\tau_{e,\rm def}$, and $\tau_{e,K}$ are the momentum relaxation rates due to phonons, (T-independent) defects, and MIs. Critically, and as reviewed in Sec. I, it is now understood that Kondo spin relaxation at MIs follows $\tau_{s,K} = \beta_K \tau_{e,K}$ with $\beta_K = 3/2$ [39,54]. The last term in Eq. (3) can thus be completely quantified, provided $1/\tau_{e,K}$ is quantified. We achieve this through use of the established Goldhaber-Gordon (G-G) phenomenological expression for the Kondo scattering rate [55,56]:

$$\frac{1}{\tau_{e,K}} = \frac{1}{\tau_{K,0}}\left(\frac{T_K'^{\,2}}{T^2 + T_K'^{\,2}}\right)^s. \tag{4}$$

$\tau_{K,0}$ here is the $\tau_{e,K}$ value in the ($T = 0$) unitary scattering limit [extractable from $\rho_N(T)$], dependent on, among other quantities, the MI concentration, T_K, and J, the conduction electron-MI exchange interaction strength [54]. A modified Kondo temperature is introduced in Eq. (4), given by $T_K' = T_K/\sqrt{2^{1/s} - 1}$, where s, the G-G exponent, is related to the magnitude of the MI spin [39,55]. $s = 0.22$ is established for Fe in Cu (where the impurity spin, $S = 1/2$), and is expected to decrease for Co, for which $S = 1$ [38,52]. Due to the low equilibrium solubility of Co in Cu, however, which has prevented extensive studies of Kondo effects in bulk $Cu_{1-x}Co_x$ alloys (they nevertheless occur in nonequilibrium thin film systems [57], such as the NLSVs studied here [38]), neither T_K nor s are well known for Co in Cu. We thus simply use $T_K = 500$ K for Co/Cu (the approximate bulk value for Co impurities in Cu [49,50,52]), and leave s as the only fit parameter in Eq. (4). $s = 0.11$ is found to describe the data, at all t_N. For Fe/Cu, T_K and s are both well known and are

thus fixed at 30 K and 0.22, respectively [41,55]. Moving to the first and second terms in Eq. (3), in initial fits we simply set $\beta_{\rm ph} = 1000$ (the CESR literature value [30,32]), $\tau_{e,\rm ph}^{-1}$ and $\tau_{e,\rm def}^{-1}$ coming directly from the T-dependent and $T \to 0$ values in Figs. 2(a) and 2(e). This leaves only $\beta_{\rm def}$ and $1/\tau_{K,0}$ as free parameters. Note here that while *T-dependent* MI spin relaxation is fully accounted for in τ_K, a classical *T-independent* term remains, contributing to $\tau_{s,\rm def}$.

Resulting fits to Eq. (3) are shown as solid lines in Fig. 3(a), providing very good quantitative descriptions of the data. Most strikingly, the T-dependent spin relaxation at MIs described by Eqs. (3) and (4) is seen to be capable of capturing not only low T decreases in τ_s^{-1} on warming (e.g., in Fe/Cu, $t_N = 200$ nm, $T_A = 300\,^\circ$C), but also the long high T tails in the upper curves in Fig. 3(a) (at higher overall spin relaxation rates). These logarithmic Kondo spin relaxation tails occur because of the very low value of β_K (3/2) compared to other spin relaxation sources such as phonons ($\beta_{\rm ph} \approx 1000$). This is most clearly visualized in Fig. 3(b), where each term in Eq. (3), due to phonons, T-independent defects, and T-dependent Kondo relaxation, is separately plotted for three illustrative devices: Fe/Cu, $t_N = 200$ nm, $T_A = 300\,^\circ$C [the lowest overall spin relaxation rate in Fig. 3(a)]; Fe/Cu, $t_N = 200$ nm, $T_A = 80\,^\circ$C (intermediate overall spin relaxation rate); and Co/Cu, $t_N = 200$ nm, $T_A = 300\,^\circ$C [just above the horizontal line dividing Co/Cu and Fe/Cu in Fig. 3(a)]. The phonon contribution to τ_s^{-1} is shown by the black solid line, increasing monotonically with T for all devices, the T-independent defect contribution by the device-dependent horizontal dashed lines, and the Kondo contribution, which decreases with T, by the colored solid lines. The key point is that because $\beta_{\rm ph} \approx 1000\ \beta_K$, the phonon contribution to τ_s^{-1} only becomes comparable to the Kondo contribution at 100–1000 K, dependent on the specific defect and MI density. It is only above this that a regime of T-linear τ_s^{-1} can be recovered, which is not reached in $T < 300$ K measurements for many samples in this work. The apparently simple expectation of a τ_s^{-1} that increases linearly with T over a wide range is in fact only seen in the lowest defect and MI density devices in this study, the exemplar being the Fe/Cu, $t_N = 200$ nm, $T_A = 300\,^\circ$C device at the bottom of Fig. 3(a). In this device the phonon contribution overpowers Kondo relaxation at around 100 K [Fig. 3(b)], giving rise to the increase in τ_s^{-1} with T seen in Fig. 3(a).

$1/\tau_{s,K}(T = 0)$ and $1/\tau_{s,\rm def} = 1/\beta_{\rm def}\tau_{e,\rm def}$, the $T = 0$ Kondo spin relaxation rate and the T-independent defect spin relaxation rate, are the two quantities extracted from the fits in Fig. 3(a), corresponding to the second and third terms in Eq. (3). [The first term is fixed by the assumed $\beta_{\rm ph} = 1000$ and the known $\tau_e(T)$.] These two contributions to τ_s^{-1} are plotted vs T_A and t_N in Figs. 4(a) and 4(b), respectively, the black points labeling the defect contribution to τ_s^{-1}, and the red points the $T = 0$ Kondo contribution. Note that an expanded data set is presented here, beyond what is shown in Fig. 3; added are the $T_A \geqslant 400\,^\circ$C data in Fig. 4(a) and $t_N > 200$ nm Py/Cu data ($T_A = 80\,^\circ$C) in Fig. 4(b). The trends of course reflect the behavior seen in Fig. 3(a), the main features being: (i) the significantly higher Kondo and defect relaxation rates in Co/Cu devices compared to Fe/Cu (by a factor of ∼10); (ii) the decrease in Kondo and defect relaxation rates with

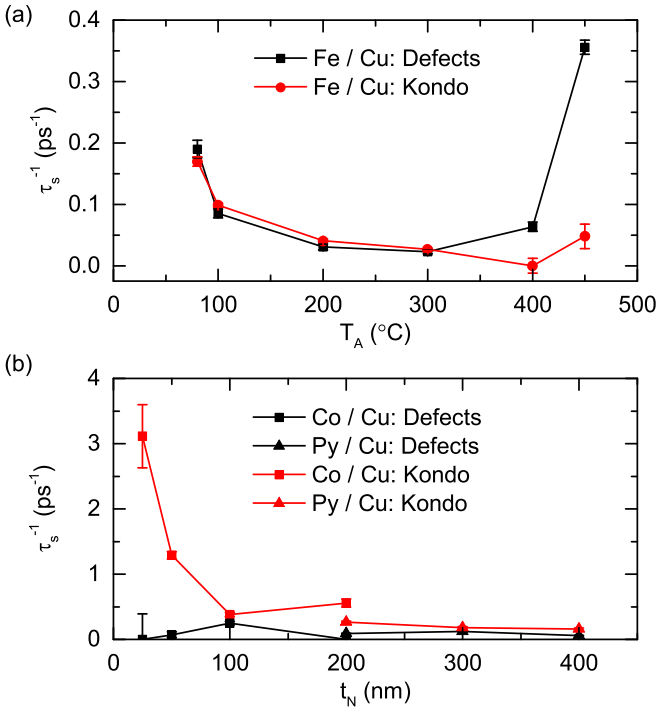

FIG. 4. Contributions to the spin relaxation rate (τ_s^{-1}) vs (a) annealing temperature T_A, and (b) channel thickness t_N. The contributions shown are the $T = 0$ Kondo spin relaxation rate ($1/\tau_{s,K,0}$, red points) and the T-independent defect spin relaxation rate ($1/\tau_{s,\rm def}$, black points). Results in (a) are for Fe/Cu NLSVs and (b) shows both Co/Cu and Py/Cu NLSVs. Error bars are standard errors on extracted fit parameters and in some cases are smaller than the points.

T_A up to ∼400 °C, before the rapid increase [Fig. 4(a)]; and (iii) the increase in Kondo relaxation at t_N below ∼100 nm [Fig. 4(b)]. The higher MI-mediated spin relaxation rate in Co/Cu devices compared to Fe/Cu ones [feature (i)] is readily explained by Eq. (4), due to the higher T_K (500 vs 30 K) and J, which result in higher Kondo scattering rates. The substantial difference in overall spin lifetime between Figs. 2(c) and 2(g) is thus understood. The evolution of active Kondo impurity density with T_A and t_N is more complex, and strongly material and deposition method dependent, but has been studied in prior work [37,38]. Important observations in the context of Fig. 4(a) are the tendency for migration of MIs toward grain boundaries with moderate annealing and Cu grain growth, reducing their effective scattering rate, and the extensive diffusion of Fe over mesoscopic distances into the Cu channel at the highest T_A [37]. With respect to Fig. 4(b), the most important prior observation is likely accumulation of MIs near the substrate/NM interface (detected via STEM/EDX imaging [37,38]), generating the increased Kondo spin relaxation rate at low t_N. The key result from analysis of $\tau_s^{-1}(T)$ based on Eq. (3) is thus that Kondo relaxation at MIs quantitatively explains the puzzling behavior of Figs. 2(c), 2(g), and 3(a), the resulting trends in Kondo and defect scattering rates being relatively simple to rationalize. As a final comment on these data we note that the similar initial response to annealing in the Kondo and defect relaxation rates [Fig. 4(a)] is likely

due to the aforementioned T-independent (non-Kondo) MI scattering.

C. Accurate determination of β_{ph} and β_{def}

In the above analysis β_{ph} was simply set at 1000, the approximate literature value from CESR measurements [30,32]. Devices in which Kondo spin relaxation is minimized, however, thus restoring the expected high T linear behavior in $\tau_s^{-1}(T)$, should enable accurate refinement of β_{ph}. This was approached in two ways: by moderate annealing of high t_N Fe/Cu NLSVs [i.e., using the lowest spin relaxation rate devices in Figs. 3(a) and 4(a)], and, following our prior work [28], by inserting thin (6 nm) Al interlayers at the FM/Cu interface. The latter are effective as Al not only does not support local moments on dissolved $3d$ transition metal impurities (thus suppressing the Kondo effect), but also has a lower diffusivity for Fe and Co compared to Cu [58]. In Fig. 3(c) we thus show "E-Y plots," i.e., τ_s^{-1} vs $\tau_{e,ph}^{-1}$ (spin relaxation rate vs momentum relaxation rate at phonons) for: Fe/Cu, $t_N = 200$ nm, $T_A = 300\,^{\circ}$C; Co/Al/Cu, $t_N = 50$ nm, $T_A = 80\,^{\circ}$C; and Fe/Al/Cu, $t_N = 200$ nm, $T_A = 80\,^{\circ}$C. Similar behavior is seen in all three cases, τ_s^{-1} increasing linearly with $\tau_{e,ph}^{-1}$ as T, the implicit variable in Fig. 3(c), is increased. This is of course nothing other than the behavior expected from Eq. (3) when the third term is small, i.e., when Kondo relaxation at MIs is minimized. The slopes of the straight line fits in Fig. 3(c) then yield β_{ph} values, the three devices shown giving 550, 670, and 990, averaging to $\beta_{ph} = 740 \pm 200$. Reassuringly, this is in reasonable agreement with both the CESR value from ultrahigh purity Cu (∼1000), as well as NLSV values (550–990) where two-step lithography [11] or deposition of FM and NM layers in separate chambers was employed [59], which could be expected to minimize MI concentrations. It can be readily visualized from Figs. 3(c) and 3(a) that Cu channels with even slightly higher MI concentration would yield weaker T dependence of τ_s^{-1}, lower slope in Fig. 3(c), and thus systematically higher β_{ph} if MIs are not properly accounted for. Reported β_{ph} values in Cu NLSVs indeed range up to 3570 [14].

β_{def} values are similarly easily extracted from the E-Y plots in Fig. 3(c). The intercept with the τ_s^{-1} axis occurs at $\tau_{e,ph}^{-1} = 0$ (i.e., $T = 0$), where the second term in Eq. (3) gives β_{def}, given the known $\tau_{e,def}$ [from $\rho_N(T \to 0)$]. This yields $\beta_{def} = 270$, 289, and 209 from the three data sets shown in Fig. 3(c). With the inclusion of the $T_A = 200$ and 400 °C data, these average to a "Kondo-minimized" $\beta_{def} = 240 \pm 50$. Following the discussion in Sec. I, it is then highly desirable to understand which specific defect type dominates this β_{def}, thus determining another of the β_i in Eq. (1) for Cu, in addition to β_{ph} and β_K. Before attempting this, it is illustrative to consider how our extracted value of β_{def} would be affected by varying MI concentrations. Figure 5(a) thus shows $\tau_s^{-1}(T = 5\,\mathrm{K})$ vs $\tau_{e,def}^{-1}$, i.e., the $T \to 0$ value of the momentum relaxation rate, on a $\log_{10} - \log_{10}$ plot, for *all* studied NLSVs, regardless of their MI spin relaxation rate. For comparison, Fig. 5(b) plots the same data as λ_N ($T = 5$ K) vs ρ_0, the residual ($T \to 0$) resistivity. In both panels the data points are color coded, using red for Fe/Cu with variable T_A, green for Co/Cu with variable t_N, dark yellow for Py/Cu with variable t_N, and blue for FM/Al/Cu NLSVs. On such low T plots the first term in Eq. (3) is negligible, meaning that straight line fits (the dashed lines) simply yield the *apparent* β_{def} ignoring Kondo scattering, i.e., ignoring the third term in Eq. (3). Three illustrative dashed lines are included in Figs. 5(a) and 5(b), corresponding to $\beta_{def} = 240$ (our accurate, "Kondo-minimized" value), $\beta_{def} = 20$ (approximately matching the Co/Cu data), and $\beta_{def} = 3/2$ (the Kondo value); the latter is the limiting case, where all defect spin relaxation is due to Kondo scattering at MIs.

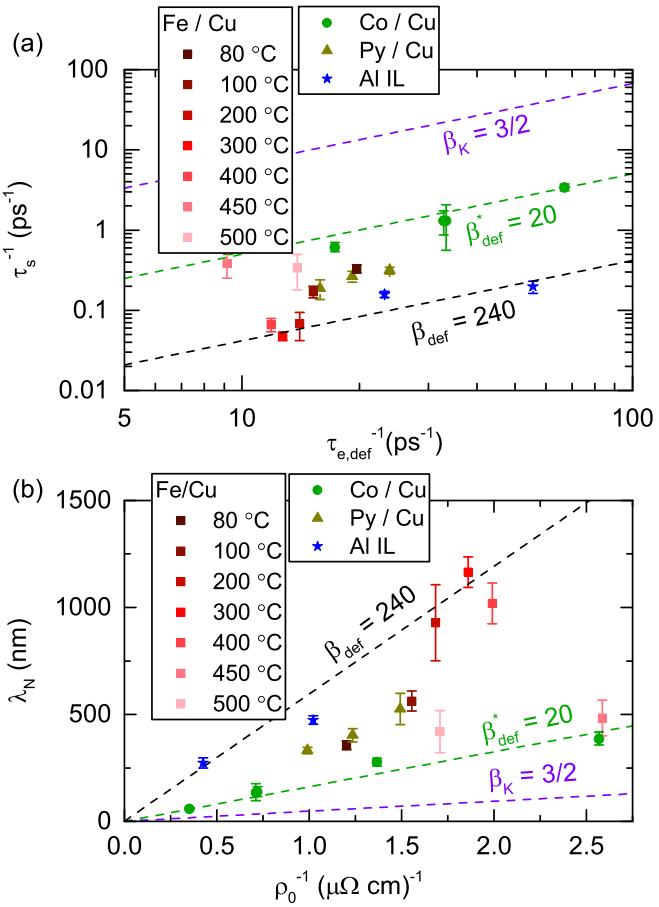

FIG. 5. (a) 5 K spin relaxation rate (τ_s^{-1}) vs $T = 0$ momentum scattering rate ($\tau_{e,def}^{-1}$) ($\log_{10} - \log_{10}$ scale) for Co/Cu, Py/Cu, Fe/Cu, and Al interlayer (IL) NLSVs. T_A values are color coded. Both T_A and t_N are implicit variables. (b) Data from (a) plotted as 5 K spin diffusion length (λ_N) vs residual ($T = 0$) resistivity (ρ_0^{-1}), on a linear scale. The dashed lines are for three values of the defect Elliott-Yafet constant: 3/2 (Kondo), 20 (the Co/Cu NLSV average), and 240 (the average in Kondo-minimized NLSVs). Error bars are standard errors on extracted fit parameters and in some cases are smaller than the data points.

Clearly the data points in Figs. 5(a) and 5(b) are remarkably widely scattered. At a given $T = 0$ momentum scattering rate the spin relaxation rate is seen to vary over about an order of magnitude, while the 5 K spin diffusion lengths span from <100 to well over 1000 nm. More meaningfully, the data essentially populate the region between the $\beta_{def} \approx 240$ and $\beta_{def} \approx 20$ dashed lines, i.e., between our accurate, Kondo-minimized value (240), and the approximate value for the Co/Cu device set (20). Close inspection confirms that the data

close to the $\beta_{\rm def} = 240$ line are indeed from NLSVs in which MI effects are minimized, specifically IL devices (blue points) and moderate T_A Fe/Cu devices. At the other extreme, Co/Cu devices, which have the highest Kondo spin relaxation rates in this work [compare for example Figs. 4(a) and 4(b), or the top and bottom regions on Fig. 3(a)] essentially cluster around the $\beta_{\rm def} = 20$ line. This $\beta_{\rm def}$ of 20 is in no way an accurate reflection of the properties of these polycrystalline Cu films, but instead a consequence of ignoring Kondo scattering at MIs in the analysis. Failure to properly understand and account for MI effects can thus have substantial impact on extracted $\beta_{\rm def}$ values, leading to inaccurate and misleading conclusions, the fundamental reason being the very low β_K at MIs. It should be noted that while this analysis provides a solid potential explanation for anomalously *low* $\beta_{\rm def}$, there are several literature values that substantially *exceed* 240, by up to an order of magnitude [14,18]. We emphasize that it is possible that our Kondo-minimized values would be even higher if MIs were entirely eradicated (which we do not claim here), and that the specific defect dominating $\beta_{\rm def}$ (see Sec. III D) may vary from study to study. As a final comment on our determined $\beta_{\rm ph}$ and $\beta_{\rm def}$ values of 740 ± 200 and 240 ± 50, we note that the two values are indeed significantly different, a conclusion that cannot be readily drawn from the widely distributed Cu NLSV literature values ($\beta_{\rm ph} = 490 - 3570$ [10,13–15,20] and $\beta_{\rm def} = 215 - 2560$ [10,11,13–15,18–20]).

D. Determination of the dominant defect type: Grain boundaries

Having highlighted the dramatic effects of Kondo scattering at MIs on spin relaxation in Cu, and having extracted reliable $\beta_{\rm ph}$ and $\beta_{\rm def}$ values in Kondo-minimized devices, we now turn to determining the dominant defect type contributing to $\beta_{\rm def}$. To do this, we examine the T_A and t_N dependence of the spin diffusion length λ_N and elastic mean-free-path $\lambda_{\rm mfp} = \sqrt{D\tau_e} = v_F\tau_e/\sqrt{3}$, as plotted Fig. 6. Shown first in Figs. 6(a) and 6(b), for Fe/Cu NLSVs, are the responses of λ_N and $\lambda_{\rm mfp}$ to T_A at illustrative measurement temperatures of 5 and 100 K, i.e., in the $T \to 0$ defect-dominated regime and at mildly elevated T. As already noted, moderate annealing at up to 300 °C induces substantial increases in λ_N, which are then lost as extensive FM/NM interdiffusion sets in at higher T_A. The increase in 5 K λ_N from 80 to 300 °C annealing temperature in fact amounts to a factor of about 3 (from ∼350 to ∼1200 nm). As can be seen from Fig. 6(b), however, the corresponding increase in 5 K $\lambda_{\rm mfp}$ is only a factor of ∼1.5, $\lambda_{\rm mfp}(T_A)$ [Fig. 6(b)] being generally weaker than $\lambda_N(T_A)$ [Fig. 6(a)]. This distinctly different response of λ_N and $\lambda_{\rm mfp}$ to annealing indicates that a single scattering mechanism does not dominate both charge and spin transport in the Cu channels studied here. It should also be noted that the significant increase in λ_N with moderate annealing is preserved even at a measurement temperature of 100 K [Fig. 6(a)], where the Kondo scattering rate $1/\tau_{s,K}$ is significantly reduced compared to 5 K. Consistently, this observation indicates that some additional scattering mechanism, beyond MI effects, is needed to explain the observed trends in Cu λ_N.

The t_N dependences of the 5 K λ_N and $\lambda_{\rm mfp}$ in Co/Cu and Py/Cu NLSVs [Figs. 6(c) and 6(d), $\log_{10} - \log_{10}$ plots]

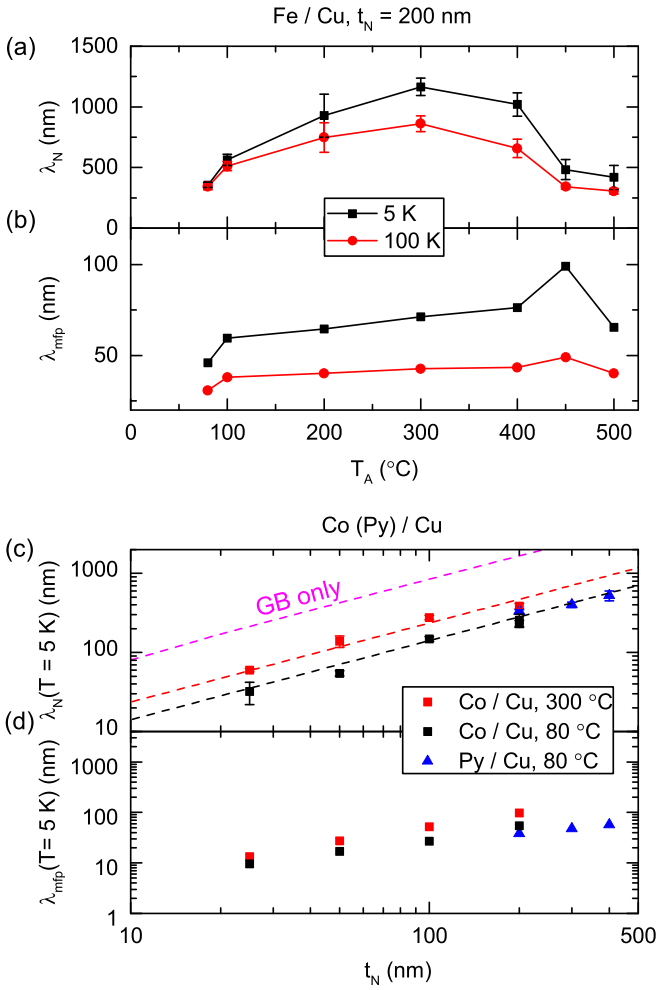

FIG. 6. Annealing temperature (T_A) dependence of (a) the spin diffusion length (λ_N), and (b) the mean-free path ($\lambda_{\rm mfp}$) in Fe/Cu NLSVs. Data are shown for both 5 and 100 K. Channel thickness (t_N) dependence at 5 K of (c) λ_N and (d) $\lambda_{\rm mfp}$ for Co/Cu and Py/Cu NLSVs (the T_A are shown), on a $\log_{10} - \log_{10}$ scale. In (c) the magenta dashed line shows the expected behavior in the absence of magnetic impurities, i.e., for T-independent defects (predominantly grain boundaries in this case) only, where $\lambda_N = \sqrt{\beta}\lambda_{\rm mfp}$ with $\beta_{\rm def} = \beta_{\rm GB} = 240$. The red and black dashed lines are straight line guides to the eye for $T_A = 300$ and 80 °C. Note that for (b) and (d) we define $\lambda_{\rm mfp} = \sqrt{D\tau_e}$, rather than $\ell_{\rm mfp} = v_F\tau_e$. Error bars are standard errors on extracted fit parameters and in some cases are smaller than the data points.

provide a further clue as to the origin of this additional scattering source. Specifically, both quantities exhibit approximately linear t_N scaling over the substantial range from 25 to 400 nm, regardless of the specific FM material or annealing conditions. For λ_N in Fig. 6(c), for example, the black and red dashed lines demonstrate linear t_N dependences for the 80 and 300 °C annealed device sets, respectively. Surface and/or interface spin relaxation is an obvious possibility to explain such t_N-linear scaling of the low T λ_N [Fig. 6(c)], but is not easily reconciled with such a strong T_A dependence [Fig. 6(a)]. Grain boundary scattering and subsequent spin relaxation is a second obvious possibility to explain t_N-linear scaling of the low T $\lambda_{\rm mfp}$ and λ_N, due to the common increase in average

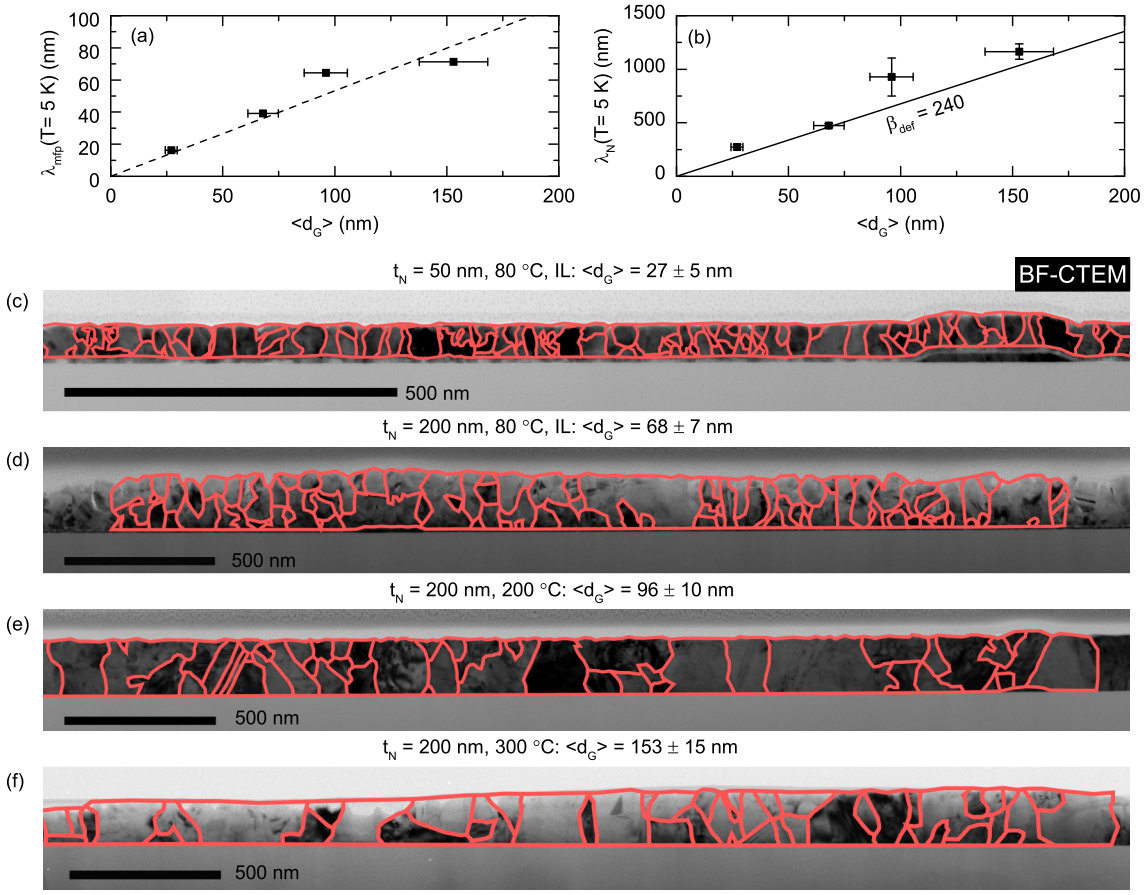

FIG. 7. Average grain size $\langle d_G \rangle$ dependence of (a) the 5 K mean-free path (λ_{mfp}) and (b) the 5 K spin diffusion length (λ_N) for Fe/Cu NLSVs. The dashed line in (a) is a straight line fit through the origin. The solid line in (b) is calculated from $\lambda_N = \sqrt{\beta_{def}}\lambda_{mfp}$, with $\beta_{def} = \beta_{GB} = 240$. Error bars correspond to one standard deviation of the grain size distribution. (c)–(f) Bright-field conventional transmission electron microscopy (BF-CTEM) images of Cu-based NLSVs. Grain outlines (red) and the resulting $\langle d_G \rangle$ are shown for: (c) Co/Al/Cu with $t_N = 50$ nm and $T_A = 80\,^{\circ}$C, (d) Fe/Al/Cu with $t_N = 200$ nm and $T_A = 80\,^{\circ}$C, (e) Fe/Cu with $t_N = 200$ nm and $T_A = 200\,^{\circ}$C, and (f) Fe/Cu with $t_N = 200$ nm and $T_A = 300\,^{\circ}$C. Extracted $\langle d_G \rangle$ are given above the images.

grain size with thickness in polycrystalline films. In fact, given the very high purity (99.999%) Cu source material employed here, and the ultrahigh vacuum deposition conditions, grain boundaries in polycrystalline films would be expected to play a key, even dominant, role in defect scattering. The T_A response [Figs. 6(a) and 6(b)] is also qualitatively consistent with grain boundary scattering, as significant grain growth would be expected at these several hundred °C annealing temperatures.

Possible proportionality between the low T values of λ_{mfp} and λ_N and the average Cu grain size $\langle d_G \rangle$ was thus tested, with the assistance of TEM imaging. The latter was achieved via FIB-based preparation of cross-sectional TEM specimens from Co/Cu and Fe/Cu NLSVs, with the FIB cut along the long axis of the Cu nanowire channel. Cross-sectional bright-field conventional TEM (BF-CTEM) imaging was thus performed *on the exact same devices* used for spin and charge transport measurements. Illustrative examples are provided in Figs. 7(c)–7(f), which show, respectively, cross-sectional BF-CTEM images of: Co/Al/Cu, $t_N = 50$ nm, $T_A = 80\,^{\circ}$C; Fe/Al/Cu, $t_N = 200$ nm, $T_A = 80\,^{\circ}$C; Fe/Cu, $t_N = 200$ nm, $T_A = 200\,^{\circ}$C; and Fe/Cu, $t_N = 200$ nm, $T_A = 300\,^{\circ}$C. Comparison between Figs. 7(c) and 7(d) thus illustrates the t_N dependence at fixed T_A, while comparison among Figs. 7(d)–7(f) illustrates the T_A dependence at fixed t_N. Considering the images, the lower t_N in Fig. 7(c) [note the different scale bar to Figs. 7(d)–7(f)] enables clear identification of a Co nanowire contact under the Cu channel, visible to the right side of the image where the Cu appears rippled. Due to the high injector-detector separation here (2000 nm) the other FM contact is out of the field of view, which is ∼1500 nm wide. The overall microstructures are qualitatively typical for polycrystalline Cu films, the BF imaging enabling facile determination of the location of the grain boundaries. These are highlighted red in Figs. 7(c)–7(f), providing the clear qualitative conclusion that $\langle d_G \rangle$ indeed increases with t_N [compare Figs. 7(c) and 7(d)] and with T_A [Figs. 7(d)–7(f)].

Quantitative analysis proceeded by manually tracing the grain boundaries [red lines in Figs. 7(c)–7(f)] and then applying automated analysis of the grain areas, which were converted to equivalent circular grain diameters d_G. The extracted d_G distribution (typically for 100 grains) was then fit to a

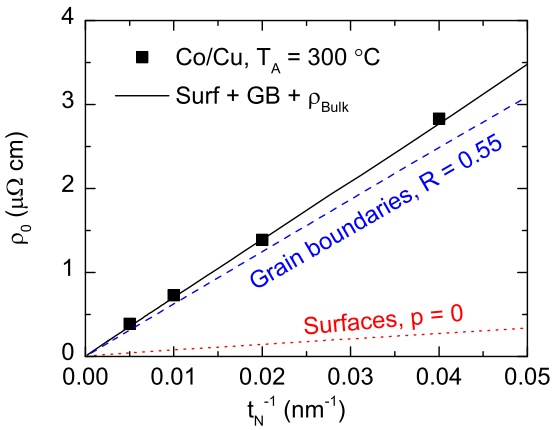

FIG. 8. Cu residual resistivity (ρ_0) vs channel thickness (t_N) for Co/Cu NLSVs annealed at $T_A = 300\,^{\circ}$C. The solid line is a fit to the model described in the text based on Mayadas-Schatzke and Fuchs-Sondheimer descriptions of surface/interface and grain boundary effects (see the Appendix also). Scattering contributions from the surface (dotted line) and grain boundaries (dashed line) are shown, along with the respective fitting parameters p and R (defined in the Appendix).

standard log-normal probability [$P(d_G)$] distribution:

$$P(d_G) = \frac{1}{d_G \sigma \sqrt{2\pi}} e^{-\frac{[\ln(d_G/\langle d_G\rangle)]^2}{2\sigma^2}}, \tag{5}$$

where σ characterizes the distribution width. The resulting $\langle d_G\rangle$ values are shown above the images in Figs. 7(c)–7(f), increasing from 27 to 68 nm as t_N is increased from 50 to 200 nm, and from 68 to 153 nm as T_A is increased from 80 to 300 °C. A quantitative test of the hypothesized proportionality between the low T $\lambda_{\rm mfp}$ and λ_N and grain size is then provided in Figs. 7(a) and 7(b), which plot the 5 K $\lambda_{\rm mfp}$ and λ_N vs $\langle d_G\rangle$. A notable simple linear proportionality is found in both cases. The dashed line in Fig. 7(a) is in fact a linear fit through the origin, yielding $\lambda_{\rm mfp}(5\,{\rm K}) = 0.53\langle d_G\rangle$. The low T mean-free path is thus not only proportional to $\langle d_G\rangle$, but is in fact close to it in absolute magnitude, further supporting the conclusion that grain boundaries are a dominant T-independent scattering source. Moreover, the solid line through the origin in Fig. 7(b) is given by $\lambda_N(5\,K) = \sqrt{\beta_{\rm def}}\lambda_{\rm mfp}$, i.e., the expectation from E-Y scaling. This is trivially derived from Eq. (3) by taking only the second term (the T-independent defect term), and using $\lambda_N = \sqrt{D\tau_s}$ and $\lambda_{\rm mfp} = \sqrt{D\tau_e}$. The solid line in Fig. 7(b) is based on our previously determined $\beta_{\rm def} = 240$ and the $\lambda_{\rm mfp}(\langle d_G\rangle)$ in Fig. 7(a) and is seen to describe the $\lambda_N(\langle d_G\rangle)$ data very well, quantitatively confirming the dominance of grain boundaries in nonmagnetic-defect-induced spin relaxation in these Cu-based devices. The determined $\beta_{\rm def}$ of 240 is thus definitively assigned to grain boundaries, meaning that three of the β_i in Eq. (1) are now known for Cu: $\beta_{\rm ph} = 740 \pm 200$, $\beta_{\rm GB} = 240 \pm 50$, and $\beta_K = 3/2$.

For completeness, we note that simple analysis of the t_N dependence of the residual resistivity ρ_0 provides yet further evidence that grain boundaries are the dominant T-independent defect in these polycrystalline Cu films. This is illustrated in Fig. 8 where ρ_0 is plotted vs $1/t_N$ for the $T_A = 300\,^{\circ}$C Co/Cu device set, testing the inverse thickness scaling frequently exhibited by metallic thin films. Linear behavior of ρ_0 with $1/t_N$ is indeed found, the black solid line being a fit to a model that combines the well-known Mayadas-Schatzkes [60] and Fuchs-Sondheimer [61,62] contributions from surface/interface and grain boundary scattering, respectively. This model is described in more detail in the Appendix. The key result, however, apparent from the dashed and dotted lines in Fig. 8, is the clear dominance of grain boundary scattering contributions over surface/interface scattering contributions. As described in the Appendix, this conclusion is arrived at even assuming zero specularity of the surface scattering (the $p = 0$ label by the dotted line in Fig. 8), i.e., the worst-case surface/interface scattering. The channel thickness effects on charge and spin transport seen throughout this paper are thus dominated by the decreasing average grain size with decreasing thickness, rather than surface/interface scattering effects, consistent with the statements above.

Note that with the known $\rho_0(1/t_N)$ from Fig. 8 (for Co/Cu), and the known $\beta_{\rm GB} = 240$, the low T form of $\lambda_N(t_N)$ in the absence of Kondo spin relaxation can be predicted from E-Y scaling. A trivial derivation gives $\lambda_N(t_N) = \sqrt{3\beta_{\rm GB}}/\rho_0(t_N)N(E_F)e^2v_F$, which is plotted as the dashed magenta line in Fig. 6(b). Kondo spin relaxation at MIs is seen to result in a nearly one order of magnitude suppression of the low T λ_N in the Co/Cu NLSV set. This occurs in devices in which $\rho_N(T)$ and $\tau_e(T)$ are essentially monotonic, meaning that conventional charge transport Kondo effects are barely detectable. Again, the ultimate reason for this is the very low $\beta_K = 3/2$, resulting in highly efficient Kondo spin relaxation at MIs in Cu.

As a final comment, we briefly consider the impact of MIs on spin transport in other technologically relevant materials, particularly semiconductors and 2D materials, e.g., graphene. A variety of magnetic impurities can play a role in spin transport in graphene, including vacancies or adatoms, such as hydrogen or fluorine. These are reviewed in Ref. [63]. As in the present case, the contribution of the impurity to the spin relaxation rate can become dominant at low T, as shown by McCreary *et al.* for the case of hydrogen impurities [64]. Fluctuating exchange fields from an adjacent magnetic layer can also induce spin relaxation [65]. In bulk semiconductor spin valves, less attention has been paid to magnetic impurities, in large part because they tend to form deep levels. This is distinct from the large body of work on magnetic semiconductors, but in that case the impurity concentration is substantial.

IV. SUMMARY

The influence of dilute magnetic impurities on spin relaxation in Cu-based nonlocal spin transport devices has been comprehensively studied, varying the ferromagnetic contact material, polycrystalline Cu channel thickness, and annealing temperature. A wide variety of microstructures and magnetic impurity concentrations and distributions result. Using recently developed theory for Kondo spin relaxation, the influence of magnetic impurities on charge and spin transport was then quantified, demonstrating their dramatic, often dominant, impact on spin relaxation rates. Temperature-dependent Kondo spin relaxation can even obscure the expected temperature dependence of phonon-limited spin lifetimes and

diffusion lengths, rendering unfeasible the extraction of phonon and defect Elliott-Yafet constants. We propose this as a major contributing factor to the wide variation in Cu Elliott-Yafet parameters reported in the nonlocal spin transport literature. Magnetic impurity effects can be minimized, however, for example with the use of Al interlayers or moderate annealing, restoring expected temperature dependencies and enabling more accurate extraction of Elliott-Yafet constants. Elliott-Yafet β values in Cu of 740 ± 200, 240 ± 50, and $3/2$ are thus now established for phonons, T-independent defects, and Kondo magnetic impurities, respectively. Through careful analyses of thickness and annealing temperature dependencies of the low temperature mean-free path and spin diffusion length, augmented with cross-sectional transmission electron microscopy, grain boundaries were then determined to be the dominant defects, establishing useful empirical relationships with grain size. These results highlight that part-per-million-level magnetic impurities can dominate spin relaxation rates in Kondo-active metals, even when the conventional charge transport Kondo effect is essentially undetectable.

ACKNOWLEDGMENTS

Work supported primarily by the National Science Foundation under Award No. DMR-1807124. Parts of this work were performed in the Characterization Facility, UMN, which receives partial support from NSF through the MSREC program. Other parts of this work were conducted in the Minnesota Nano Center, which is supported by the NSF through the National Nano Coordinated Infrastructure Network, Award No. NNCI-1542202. L.O'B. acknowledges support from the UK EPSRC, Grant No. EP/P005713/1.

APPENDIX

T-independent defect scattering contributions due to grain boundaries and surfaces/interfaces were modeled assuming Mattheissen's rule:

$$\rho_N = \rho_{\text{bulk}} + \rho_{\text{surf}} + \rho_{\text{GB}}, \tag{A1}$$

where ρ_{bulk} is the resistivity in the absence of grain boundaries and surfaces (which we leave as a free parameter), ρ_{surf} is the contribution to the resistivity due to surface/interface scattering, and ρ_{GB} is the contribution to the resistivity due to grain boundary scattering. This is applied to the data of Fig. 8 to fit the t_N dependence of the residual resistivity ρ_0. Following Mayadas and Schatzke [60], the surface contribution is given by

$$\rho_{\text{surf}} = \rho_{\text{bulk}} \left[1 - \frac{3}{2k}(1-p) \int_1^\infty (x^{-3} - x^{-5}) \frac{1-e^{-kx}}{1-pe^{-kx}} dx \right]^{-1}, \tag{A2}$$

where $k = t_N/\lambda_0$, p is the specularity of the surface scattering, and the bulk-limit mean-free path $\lambda_0 = \sqrt{3}/N(E_F)e^2 v_F \rho_{\text{bulk}}$. Following Fuchs and Sondheimer [61,62], the grain boundary contribution is given by

$$\rho_{\text{GB}} = \rho_{\text{bulk}} \left[1 - \frac{3}{2}\alpha_G + 3{\alpha_G}^2 - 3{\alpha_G}^3 \ln(1 + {\alpha_G}^{-1}) \right]^{-1},$$

$$\alpha_G = \frac{\lambda_0 R}{d_G(1-R)}, \tag{A3}$$

where R is the grain boundary scattering probability.

In Fig. 8 the solid line is a fit to Eq. (A1) assuming perfectly diffuse surfaces ($p = 0$). This corresponds to the maximum possible surface contribution, leaving R and ρ_{bulk} as free parameters. The result from the solid line is $R = 0.55$, in good agreement with previously reported values for Cu [9,66]. The corresponding ρ_{surf} (dotted line) and ρ_{GB} (dashed line) are also shown in Fig. 8. Even assuming the maximum diffuse surface scattering contribution (i.e., $p = 0$), we find that the scaling of ρ_0 with $1/t_N$ in these devices can only be accounted for with a dominant grain boundary scattering contribution, consistent with the other results in this paper.

[1] M. Yamada, D. Sato, N. Yoshida, M. Sato, K. Meguro, and S. Ogawa, IEEE Trans. Magn. **49**, 713 (2013).
[2] Y. K. Takahashi, S. Kasai, S. Hirayama, S. Mitani, and K. Hono, Appl. Phys. Lett. **100**, 052405 (2012).
[3] M. Takagishi, K. Yamada, H. Iwasaki, H. N. Fuke, and S. Hashimoto, IEEE Trans. Magn. **46**, 2086 (2010).
[4] M. Johnson and R. H. Silsbee, Phys. Rev. Lett. **55**, 1790 (1985).
[5] F. J. Jedema, A. T. Filip, and B. J. van Wees, Nature (London) **410**, 345 (2001).
[6] G. Mihajlović, S. I. Erlingsson, K. Výborný, J. E. Pearson, S. D. Bader, and A. Hoffmann, Phys. Rev. B **84**, 132407 (2011).
[7] H. Idzuchi, Y. Fukuma, L. Wang, and Y. Otani, Appl. Phys. Lett. **101**, 022415 (2012).
[8] H. Zou and Y. Ji, Appl. Phys. Lett. **101**, 082401 (2012).
[9] S. Rakheja, S.-C. Chang, and A. Naeemi, IEEE Trans. Electron Devices **60**, 3913 (2013).
[10] E. Villamor, M. Isasa, L. E. Hueso, and F. Casanova, Phys. Rev. B **88**, 184411 (2013).
[11] E. Villamor, M. Isasa, L. E. Hueso, and F. Casanova, Phys. Rev. B **87**, 094417 (2013).
[12] S. Chen, H. Zou, C. Qin, and Y. Ji, Appl. Phys. Express **7**, 113001 (2014).
[13] J. T. Batley, M. C. Rosamond, M. Ali, E. H. Linfield, G. Burnell, and B. J. Hickey, Phys. Rev. B **92**, 220420(R) (2015).
[14] Y. Cai, Y. Luo, C. Zhou, C. Qin, S. Chen, Y. Wu, and Y. Ji, J. Phys. D: Appl. Phys. **49**, 185003 (2016).
[15] F. J. Jedema, M. S. Nijboer, A. T. Filip, and B. J. van Wees, Phys. Rev. B **67**, 085319 (2003).
[16] S. O. Valenzuela and M. Tinkham, Appl. Phys. Lett. **85**, 5914 (2004).
[17] Y. Ji, A. Hoffmann, J. S. Jiang, and S. D. Bader, Appl. Phys. Lett. **85**, 6218 (2004).
[18] S. Garzon, I. Žutić, and R. A. Webb, Phys. Rev. Lett. **94**, 176601 (2005).
[19] T. Kimura, T. Sato, and Y. Otani, Phys. Rev. Lett. **100**, 066602 (2008).

[20] X. J. Wang, H. Zou, and Y. Ji, Phys. Rev. B **81**, 104409 (2010).
[21] G. Mihajlović, J. E. Pearson, S. D. Bader, and A. Hoffmann, Phys. Rev. Lett. **104**, 237202 (2010).
[22] M. Erekhinsky, A. Sharoni, F. Casanova, and I. K. Schuller, Appl. Phys. Lett. **96**, 022513 (2010).
[23] N. Poli, M. Urech, V. Korenivski, and D. B. Haviland, J. Appl. Phys. **99**, 08H701 (2006).
[24] A. Fert and P. M. Levy, Phys. Rev. Lett. **106**, 157208 (2011).
[25] Y. Otani and T. Kimura, Philos. Trans. A. Math. Phys. Eng. Sci. **369**, 3136 (2011).
[26] R. Godfrey and M. Johnson, Phys. Rev. Lett. **96**, 136601 (2006).
[27] A. Fert and O. Jaoul, Phys. Rev. Lett. **28**, 303 (1972).
[28] L. O'Brien, M. J. Erickson, D. Spivak, H. Ambaye, R. J. Goyette, V. Lauter, P. A. Crowell, and C. Leighton, Nat. Commun. **5**, 3927 (2014).
[29] R. J. Elliott, Phys. Rev. **96**, 266 (1954).
[30] F. Beuneu and P. Monod, Phys. Rev. B **18**, 2422 (1978).
[31] Y. Yafet, Solid State Phys. **14**, 1 (1963).
[32] P. Monod and F. Beuneu, Phys. Rev. B **19**, 911 (1979).
[33] J. Fabian and S. Das Sarma, Phys. Rev. Lett. **81**, 5624 (1998).
[34] J. Fabian and S. Das Sarma, Phys. Rev. Lett. **83**, 1211 (1999).
[35] P. Monod and S. Schultz, J. Phys. **43**, 393 (1982).
[36] C. Zhou, F. Kandaz, Y. Cai, C. Qin, M. Jia, Z. Yuan, Y. Wu, and Y. Ji, Phys. Rev. B **96**, 094413 (2017).
[37] L. O'Brien, D. Spivak, J. S. Jeong, K. A. Mkhoyan, P. A. Crowell, and C. Leighton, Phys. Rev. B **93**, 014413 (2016).
[38] J. D. Watts, J. S. Jeong, L. O'Brien, K. A. Mkhoyan, P. A. Crowell, and C. Leighton, Appl. Phys. Lett. **110**, 222407 (2017).
[39] K.-W. Kim, L. O'Brien, P. A. Crowell, C. Leighton, and M. D. Stiles, Phys. Rev. B **95**, 104404 (2017).
[40] K. Hamaya, T. Kurokawa, S. Oki, S. Yamada, T. Kanashima, and T. Taniyama, Phys. Rev. B **94**, 140401(R) (2016).
[41] J. A. Mydosh, *Spin Glasses: An Experimental Introduction* (Taylor and Francis, London, 1993).
[42] G. Gruner and A. Zawadowski, Rep. Prog. Phys. **37**, 1497 (1974).
[43] J. Kondo, *The Physics of Dilute Magnetic Alloys* (Cambridge University Press, Cambridge, 2012).
[44] L. O'Brien, D. Spivak, N. Krueger, T. A. Peterson, M. J. Erickson, B. Bolon, C. C. Geppert, C. Leighton, and P. A. Crowell, Phys. Rev. B **94**, 094431 (2016).
[45] S. Takahashi and S. Maekawa, Phys. Rev. B **67**, 052409 (2003).
[46] T. Valet and A. Fert, Phys. Rev. B **48**, 7099 (1993).
[47] J. Bass and W. P. Pratt, J. Phys.: Condens. Matter **19**, 183201 (2007).
[48] C. Kittel, *Introduction to Solid State Physics*, 6th ed. (Wiley, New York, 1986).
[49] W. Wei and G. Bergmann, Phys. Rev. B **37**, 5990 (1988).
[50] N. Néel, J. Kröger, R. Berndt, T. O. Wehling, A. I. Lichtenstein, and M. I. Katsnelson, Phys. Rev. Lett. **101**, 266803 (2008).
[51] M. A. Blachly and N. Giordano, Phys. Rev. B **49**, 6788 (1994).
[52] B. Surer, M. Troyer, P. Werner, T. O. Wehling, A. M. Läuchli, A. Wilhelm, and A. I. Lichtenstein, Phys. Rev. B **85**, 085114 (2012).
[53] A. Fert, A. Friederich, and A. Hamzic, J. Magn. Magn. Mater. **24**, 231 (1981).
[54] J. Kondo, Prog. Theor. Phys. **32**, 37 (1964).
[55] M. Grobis, I. G. Rau, R. M. Potok, and D. Goldhaber-Gordon, in *Handbook of Magnetism and Advanced Magnetic Materials* (John Wiley & Sons, Chichester, UK, 2006), p. 50.
[56] D. Goldhaber-Gordon, J. Göres, M. A. Kastner, H. Shtrikman, D. Mahalu, and U. Meirav, Phys. Rev. Lett. **81**, 5225 (1998).
[57] J. R. Childress and C. L. Chien, Phys. Rev. B **43**, 8089 (1991).
[58] G. Salje and M. Feller-Kniepmeier, J. Appl. Phys. **49**, 229 (1978).
[59] Y. Fukuma, L. Wang, H. Idzuchi, S. Takahashi, S. Maekawa, and Y. Otani, Nat. Mater. **10**, 527 (2011).
[60] A. F. Mayadas and M. Shatzkes, Phys. Rev. B **1**, 1382 (1970).
[61] K. Fuchs, Math. Proc. Cambridge Philos. Soc. **34**, 100 (1938).
[62] E. H. Sondheimer, Adv. Phys. **1**, 1 (1952).
[63] W. Han, R. K. Kawakami, M. Gmitra, and J. Fabian, Nat. Nanotechnol. **9**, 794 (2014).
[64] K. M. McCreary, A. G. Swartz, W. Han, J. Fabian, and R. K. Kawakami, Phys. Rev. Lett. **109**, 186604 (2012).
[65] S. Singh, J. Katoch, T. Zhu, K. Y. Meng, T. Liu, J. T. Brangham, F. Yang, M. E. Flatté, and R. K. Kawakami, Phys. Rev. Lett. **118**, 187201 (2017).
[66] T. Sun, B. Yao, A. P. Warren, K. Barmak, M. F. Toney, R. E. Peale, and K. R. Coffey, Phys. Rev. B **81**, 155454 (2010).